

The new small angle X-ray scattering beamline for materials research at PETRA III: SAXSMAT beamline P62.

S. Haas^{a*}, X. Sun^a, A.L. Conceicao^a, J. Horbach^a, S. Pfeffer^a

^a Deutsches Elektronen-Synchrotron DESY, Notkestr. 85, 22607 Hamburg, Germany

*Correspondence e-mail: sylvio.haas@desy.de

Synopsis:



Abstract:

The SAXSMAT beamline P62 (Small Angle X-ray Scattering beamline for Materials Research) is a new beamline at the high-energy storage ring PETRA III at DESY PETRA III. This beamline is dedicated to combined small- and wide-angle X-ray scattering (SAXS/WAXS) techniques for both soft and hard condensed matter systems. It works mainly in transmission geometry. The beamline covers an energy range from 3.5 keV to 35.0 keV, which fulfills the requirements of the user community to perform anomalous scattering experiments. Mirrors are used to reduce the intensity of higher harmonics. Furthermore, the mirrors and 2D compound refracting lenses can focus the beam down to a few micrometers at the sample position. This option with the high photon flux enables also SAXS/WAXS tensor tomography experiments at this new beamline to be performed in a relatively short time. The first SAXS/WAXS pattern was collected in August 2021, while the first user experiment was carried out two months later. Since January 2022 the beamline is in regular user operation mode. In this paper, the beamline optics and the SAXS/WAXS instrument are described as well as two examples are shortly shown.

Keywords:

SAXS, WAXS, SAXS tensor tomography, SAXS-TT, computed tomography, anomalous scattering, ASAXS

1 Introduction

At the PETRA III storage ring, two dedicated small-angle X-ray scattering beamlines are operational for several years successfully. The beamline P03 focused on grazing incidence small angle X-ray

1 scattering (GISAXS) and microfocus applications (Buffet *et al.*, 2012; Krywka *et al.*, 2012). The second
2 beamline P12 operated by the EMBL (European macromolecular biological laboratory) is highly
3 optimized for BioSAXS applications (Blanchet *et al.*, 2015). To complete the portfolio of SAXS-related
4 techniques at the PETRA III facility and to relax the overbooking of the highly requested SAXS
5 beamlines at PETRA III a new SAXS dedicated beamline was planned, installed, and commissioned
6 over the last three years. The additional SAXS-related beamline was realized within the successfully
7 finished PETRA III extension project (Drube *et al.*, 2016; Franz *et al.*, 2006).

8 The new beamline called SAXSMAT beamline P62 (Small Angle X-ray Scattering beamline for
9 Materials Research) is dedicated to combined small- and wide-angle X-ray scattering (SAXS/WAXS)
10 for soft and hard condensed matter systems mainly in transmission geometry. This beamline allows
11 for two advanced SAXS techniques: anomalous small angle X-ray scattering (ASAXS) (Haas *et al.*,
12 2010, 2013; Sztucki *et al.*, 2011; Hoell *et al.*, 2009; Tatchev, 2008) and SAXS tensor tomography
13 (SAXS-TT) (Liebi *et al.*, 2015, 2018; Schaff *et al.*, 2015; Guizar-Sicairos *et al.*, 2020; Conceição *et al.*,
14 2020; Jensen *et al.*, 2011). Special sample environments for both techniques have been developed
15 and realized at the beamline and will be explained partially in this paper. The ASAXS method implies
16 that the X-ray energy can be tuned continuously within a few seconds with a reliable and stable
17 measurement of the incoming photon flux and transmitted beam intensity. To have access to as
18 many X-ray absorption edge energies as possible the beamline optics was chosen such that the
19 energy can be continuously tuned from 3.5 to 35.0 keV. This allows reaching at least one absorption
20 edge for all elements with Z larger than 19 (potassium). The second major technique of SAXS-TT is
21 extremely demanding on the data-taking and handling strategy. At the SAXSMAT beamline, a
22 continuous scan (on-the-fly data taking) has been implemented using an FPGA-based controller for
23 synchronization of the continuous motion and the data taking. With this method, a common SAXS-TT
24 data set can easily reach more than 1 million 2D SAXS and WAXS patterns collected within a couple
25 of hours. Depending on the sample and the information wished different imaging approaches can be
26 implemented to generate images from 4D (2D real space + 2D reciprocal space) to 6D (3D real space
27 + 3D reciprocal space). Furthermore, conventional time-resolved and high throughput combined
28 SAXS/WAXS experiments with millisecond time resolution can be conducted at the SAXSMAT
29 beamline as well.

30 The first monochromatic X-ray beam in the experimental hutch was achieved in August 2021. Two
31 months later the first regular external user experiment has been carried out successfully. Since then,
32 the beamline started the normal regular user operation with a few longer periods for further
33 optimization of existing components and installation of missing equipment. Since January 2022 the
34 beamline is in full user operation mode. Within this paper, the beamline layout and performance will

be discussed and finally, a few preliminary examples will be shown to highlight the potential of the beamline.

2 Beamline overview

The generic beamline layout including optics and end-station is shown in Figure 1. The photon source of the beamline is a U32 undulator with a peak brilliance of 1.4×10^{20} (photons/s/mrad²/0.1% BW) at 7 keV. The monochromatization is realized by a cryo-cooled double-crystal monochromator (DCM) with Si(111) and Si(311) pairs depending on the requested energy resolution in the range of 3.5 keV - 35.0 keV. For harmonic suppression, two vertical deflecting flat mirrors with B₄C, Rh, and Pt stripes are used. The incoming X-ray beam can be focused either on the sample position or on the SAXS detector by bending the second mirror or using the cylindrical stripe of the mirrors, or by using different numbers of 2D Beryllium lenses. At 12 keV 120 mA storage ring current, the beamline can reach a peak flux of $\sim 1.2 \times 10^{13}$ photons/s at the sample position. The end station of the beamline consists of a permanently installed SAXS/WAXS instrument with a flexible sample environment area. The key parameters of the beamline specification in terms of optics are given in Table 1.

2.1 Photon Source

Table 2 summarizes the specification of the U32 undulator (Schöps *et al.*, 2016). The U32 undulator has a period length of 31.4 mm with a peak magnetic field of 0.91 T. The insertion device has 61 periods resulting in a total length of the insertion device of 2m. The energy of the 1st harmonic is at 2.4 keV. The total power of the U32 for this configuration is 3.8 kW with an on-axis power density of 80 W/mrad². The brilliance as a function of the X-ray energy and harmonic is shown in the supplementary information (Figure S 1). To fulfill the low divergence criteria for the SAXS technique the undulator cell in the storage ring is configured as high β -mode, yielding $140.0 \times 5.6 \mu\text{m}^2$ source size and $7.9 \times 4.1 \mu\text{rad}^2$ (RMS) divergence at 10 keV photon energy. An important mode of the beamline operation will be continuous energy scans of roughly 1.5 keV range within about 1 minute. That requires that the undulator gap can be continuously scanned at a certain speed. This speed depends on the starting energy and harmonic. The fastest speed for the gap scan is in the range of 100 $\mu\text{m/s}$ for scans around 8 - 10 keV. The current design of the PETRA III extension undulator frames allows a gap scan speed of several hundred $\mu\text{m/s}$, with an option to adapt the gap scan speed during the scan movement.

2.2 Front-end

The front end of the beamline contains a white beam aperture, a white beam high power slit system (vertical and horizontal) followed by an absorber (Schulte-Schrepping *et al.*, 2016). The absorber unit has two positions: a 300 μm thick glassy carbon sheet and an empty position (no absorber). The last

element in the front end is the optics beam shutter. In addition, several beam position monitors are placed behind each important component in the front-end section. These beam monitors are based on a CCD camera (charge-coupled device) that looks at a diamond sheet with an etched cross in the center. Each screen can be moved in and out of the beam.

2.3 Beamline optics

The first optical element after the front-end section is a diamond window coupled with a CCD camera. This window separates the ultra-high vacuum parts and acts as a beam position screen at the beginning of the optics hutch. The first active optical element is a high heat load cryo-cooled double crystal monochromator (DCM), followed by a white beam absorber. The next components are two vertical deflecting flat mirrors for efficient suppression of harmonics. These mirrors can also be used for focusing. Downstream of the mirrors, two slit systems have been installed with a 2D-Be lens translocator unit in between. The optics section has been divided into several ultra-high vacuum sections for easier maintenance work. The optics section also contains several beam position screens based on a CCD camera looking onto a diamond sheet with an etched cross in the center. These screens can be moved out of the beam during normal user operation.

2.3.1 Cryo-cooled double crystal monochromator

The cryo-cooled double crystal monochromator (DCM) of beamline P62 is the standard PETRA III high-heat-load monochromator with some modifications to further improve the monochromatic beam stability (Schulte-Schrepping *et al.*, 2013). Extensive work has been done to improve the overall stability of the monochromators for PETRA III extension. Stability increased especially for the cryo-cooling components in the DCM vessel after these issues had been identified during systematic tests and modification at PETRA III (Sergueev *et al.*, 2016). Measures were taken by the company FMB-Oxford to improve these issues (Kristiansen *et al.*, 2015).

In Figure 2(a) a photograph of the inner part of the installed DCM is shown (built by FMB-Oxford). A sketch of the fundamental principle of the DCM including the naming of the degree of freedom is shown in Figure 2(b). The monochromator is fixed-exit with an adjustable fix beam offset in the range of 21 mm – 23 mm upwards. The accessible energy range of the DCM is 3.5 keV to 35.0 keV using the Si(111) reflection. To increase the energy resolution as well as get to higher X-ray energies an additional Si(311)-pair of crystals is implemented. The fixed exit is realized by a vertical (C2z) and a horizontal (C2x) translation of the second crystal. The surface of the first crystal stays within the rotation axis and C1pitch is identical to the Bragg angle. Because both crystal cages are mounted on one backplane, the second crystal is rotated simultaneously with the first one. This means that C2pitch only affects the angle between the first and second crystal. Both pitch and roll of the second

crystal can be fine-tuned separately for alignment purposes, whereas the pitch has an additional piezo-driven stage for feedback and detuning of the second crystal concerning the first crystal. A modification compared to the latest version of the PETRA III extension DCMs is the shorter longitudinal translation C2x of the second crystal by roughly 30%. This reduction can be realized due to the narrower energy range of 3.5 keV – 35.0 keV with the Si (111) reflection while keeping the fixed exit. The shorter translation allows a slightly compacter design of the inner part of the monochromator, which makes the monochromator more stable. The specifications of the travel range, repeatability, and step resolution of the P62 DCM are summarized in Table 3.

2.3.2 The vertical deflecting double mirror system

Two separate mirrors in vertical deflecting geometry are installed to suppress higher harmonics efficiently and keep the beam parallel to the white beam. To be able to use the mirrors over the entire energy range three flat stripes with B₄C, Rh, and Pt coatings respectively as well as one cylindrical stripe either B₄C or Rh are used on both mirrors. The reflectivity curves of a double mirror system as a function of X-ray energy and incidence angle (pitch) for the different coatings are shown in the supplementary information (Figure S 2). For energies between 3.5 keV and 13.0 keV, the B₄C coating is used with a reflectivity of ~99.8%. For the middle energy range of 12.0 keV to 21.0 keV, the Rh coating is used with a reflectivity of ~ 94%. For the higher energy range from 20.0 keV to 35.0 keV, the Pt coating can be used with a reflectivity of ~80%. An operation without the mirrors can be realized but is not the default beamline operation mode, because higher harmonic suppression is needed for high-resolution scattering experiments.

In addition to the flat stripes, the 1st mirror has one cylindrical B₄C stripe, and the 2nd mirror has one cylindrical Rh stripe, respectively. The sagittal radius of both cylindrical stripes is 73 mm and 56 mm for focusing the beam horizontally onto the sample position. The theoretical reachable horizontal beam size is in the order of 110 μm with a divergency of 23.7 μrad. Experimentally, a horizontal beam size of 125 μm at the sample position has been measured indicating a good agreement with the calculated one. The second mirror can be tangentially bent with a bending radius from 11.5 km down to 8.6 km which allows adjusting the focal length to match the mirror to the sample position for the different pitch angles of the mirror.

2.3.3 CRL Transfocator

To increase the focusing capabilities of the beamline 2D-Be compound refractive lenses (CRLs) are installed at two positions. In the optics hutch a lens transfocator equipped with 90x radius of 500 μm, 3x radius of 1500 μm, 1x radius of 2500 μm, and 1x radius of 5000 μm will be installed. The number of lenses can be varied based on the required focal length at a given X-ray energy. To have a fine

adjustment of the focal length the whole transfocator can be translated in beam direction up to 1m. This transfocator allows focusing either on the sample position or on the SAXS detector far away from the sample in both directions. This device is still in the commissioning phase. A second 2D-Be lens transfocator is installed in the experimental hutch roughly 800 mm before the sample position. This transfocator can be equipped manually with up to 30x 2D-Be lenses with a radius of 50 μm . This lens system is used especially for the SAXS imaging techniques allowing a focus size of roughly $10 \times 10 \mu\text{m}^2$ on the sample position. Here the round beam shape is realized by slightly defocusing the beam vertically with the mirror system to match the horizontal beam size. This system is fully commissioned and in regular use for the SAXS-tensor tomography experiments.

2.4 End-station

The first element in the experimental hutch is again a diamond window attached with a CCD camera on the side. This window separates the ultra-high vacuum ($\sim 1 \times 10^{-9}$ mbar) path in the optics hutch from the high vacuum (1×10^{-4} mbar) path in the experimental hutch. Shortly behind the window, the 1st slit system from JJ-X-rays is installed. The next component is a precision X-ray attenuation unit (ADC ABS-300) based on moving metal foils in and out of the beam. A wide range of attenuation across the entire energy range is realized by 11 different optimized metal foils: Al (20, 40, 80, 160, 200, 400, 800, 1600 μm), Cu (7 μm), Mo (25 μm), and W (2 mm). The last slot (2 mm W) can be used as a slow shutter absorbing all photons. The control of the unit is based on an SPS system from Beckhoff that can be easily controlled via a tango server. Further downstream an optical mirror inside a vacuum cube can be moved into the X-ray beam position. This mirror is used to couple a green laser into the system to mimic the X-ray beam path. The laser unit is mounted outside the vacuum chamber and has 5 degrees of freedom for aligning the laser beam path to the X-ray beam path. Once both paths are matching only the cube with the mirror inside must be moved 10 mm to the side and the X-ray can pass the unit without interaction with the laser setup. The next component is a fast shutter unit. The fast shutter is based on a Galvano motor inside a vacuum cube. On the Galvano motor head, two special custom-made Densimet® pieces (rhombus-shaped) are mounted. A total maximum rotation of 40 degrees is sufficient to either block or fully open an aperture of 2.5 mm. The open and closing time is 2.2 ms for a total travel range of 40 degrees. Depending on the actual beam size the attenuation of the full beam is faster than 2.2 ms. A feedback analog signal from the Galvano motor is fed into the control system to wait for the shutter to be opened or closed completely. Due to the small aperture of this unit, the vacuum cube with the shutter inside can be vertically and horizontally adjusted via stepper motors. Further downstream a beam intensity monitor is installed. A windowless photodiode (Hamamatsu, S1337-21) inside a vacuum cube is collecting light and fluorescence originating from a nitrogen-doped CVD diamond

sheet (50 μ m thickness) that can be moved at 45 degrees into the beam axis. As a cross-check of the beam intensity, an additional ionization chamber filled with nitrogen (1 bar) is installed in front of the guard slit (JJ-Xray).

For the sample environments either from the users or the beamline equipment an optical breadboard table (900 mm x 900 mm) is installed at the nominal sample position. This table can move 250 kg 300 mm up/down. Downstream of the sample table, the in-house constructed/built SAXS/WAXS instrument is permanently installed.

2.4.1 SAXS/WAXS-instrument

Figure 3 shows a 3D CAD model of the realized SAXS/WAXS instrument. The SAXS instrument is composed of a 13 m long and 1 m diameter stainless steel tube (304L) with inside motorized translation stages for the SAXS detector and beamstops. The wall thickness is 15 mm to ensure low vibration and no deformation while moving the SAXS detector system inside the tube system. The different vacuum tube sections (1m and 2m long) have been manufactured by Pfeiffer Vacuum including support brackets inside for mounting the inside translation system. The translation system inside has been built internally at DESY. The vacuum tube system is supported underneath by an aluminum-profile frame system from the company Rose+Krieger. Inside the tube, a rail system allows continuous movement of the SAXS detector system from 1.9 m to 13.0 m to the sample position. The guiding rails are from the company HEPCO Motion and are optimized for vacuum applications. The motorized motion is realized by two parallel rack and pinion drive systems in combination with electronically synchronized stepper motors. In Figure 3 (c) the water-cooled stepper motors can be seen behind the detector system (the yellow items).

The SAXS detector, an Eiger2 X 9M (Dectris[®]) is mounted on a secondary translation stage for off-centering the detector horizontally and vertically, such that the direct beam can hit the detector either in the center or the lower left/right corner. By this option, the accessible q-range for isotropic scattering samples can be nearly doubled.

In front of the SAXS detector, two large 2mm thick Densimet[®] plates are installed as a protective cover during X-ray beam alignment tasks (dark green items in Figure 3 (c)). These plates are motorized with individually driven stepper motors. Direct in front of this protecting cover one beam-stop unit with two separate motorized beam-stops is installed. There is an option to install two more identical beam-stop units with different beam-stops in front of it. Currently, a 4.5 mm and a 6.0 mm round active beam-stop are used. These beam-stops are based on a Densimet[®] cylinder with a Ce:Gd₃Al₂Ga₃O₁₂ crystal inside (Advatech UK Limited). Inside the metal supporting stick a 600 μ m glass fiber is used to guide the produced visible light (wavelength: 530 nm) from the crystal to the outside of the vacuum vessel, where the light signal will be converted into an electrical voltage signal

(Femto: 200 MHz Variable Gain Photoreceiver Series OE-300). The intensity of the signal is proportional to the X-ray beam flux.

In front of the SAXS tube, a DN500 high vacuum pendulum isolation valve (VAT Vakuumventile AG) is installed to separate the SAXS vacuum system from the sample environment vacuum system while mounting the vacuum sample setup or/and changing the samples within this vacuum sample chamber. From the nominal sample position to the large valve, a customized vacuum cone is installed. Below this cone, the Eiger2X 4M-DESY detector from Dectris® is placed as the WAXS detector. The shape of this detector, especially the top housing shape, matches the vacuum cone shape to reduce the gap between the SAXS and WAXS signal. Another modification of the customized Eiger2X 4M-DESY is that the first active pixel row is just 7 mm below the upper housing of the detector, which further reduced the gap between the SAXS and WAXS signal.

A summary of the key specification of the SAXS/WAXS instrument is given in Table 4.

2.4.2 Sample environment

The beamline has been designed such, that the sample environment area is a free space for mounting user equipment or special environments from the beamline. At the sample position area, an optical breadboard table (900 x 900 mm²) is permanently installed. This table can lift roughly 250 kg. The user equipment can be placed on this table and adjusted in height to match the X-ray beam height. At the beamline, several environments are available, such as a large and a small chamber housing different setup. A large chamber that can be filled with He gas or evacuated to 1×10^{-4} mbar. This chamber houses a coarse motion system with 4 translation degrees of freedom. In Figure 4 (a) the chamber is shown and in (b) a detailed 3D CAD model of the coarse motion system. This setup is mainly used for the SAXS/WAXS tensor tomography experiments in combination with an additional fine motion scanning system from SmarAct®. For standard ASAXS/AWAXS experiments, a small vacuum chamber (Figure 4) is available that has two translation degrees of freedom. This small chamber can be directly connected to the SAXS/WAXS instrument without any extra window. Therefore, a very low scattering background can be achieved with this setup.

To mount and align small user equipment that cannot be placed inside a vacuum a second identical coarse motion system is available that can be operated in air and can be mounted on the optical breadboard table. This coarse motion system can handle equipment with a maximum of 5kg weight. Besides the sample environments, the beamline develops user-accessible equipment for in situ and operando experiments. The equipment often used at the beamline includes a capillary heater that can reach a temperature up to 1000°C with a gas flow connection, a setup with five individually controlled heaters up to a temperature of 500 °C, a capillary flow through cell connected to a syringe pump system, and a tensile stage with forces from 0.01N – 600N.

2.4.3 Control system

The control of the beamline is based on Tango Device Server (TANGO, 2023) and Sardana (Sardana, 2023) (Sardana, 2023). Respectively, the command line interface called “spock” is used to communicate with Sardana or we can use custom graphical user interfaces written in Python using the PyTango (PyTango, 2023) package to access the tango devices and the Sardana macro server. In Figure 5 an overview of the acquisition system is shown. The core of this system is two PiLCs (Raspberry Pi Logic Controller). The basic components of a PiLC are an embedded PC, an FPGA chip, and IO Cards interfaces for digital and analog signals. During operation, the embedded PC loads the firmware, which has been developed for a specific application, into the FPGA, activates it, and provides access to the FPGA registers. This device has been developed in-house at DESY. The user interacts with these devices via the Tango server and Sardana macros. The master PiLC generates signal GATES that can be used to trigger the exposure of different devices such as the exposure of the SAXS and WAXS detector or the acquisition of the slave PiLC. The slave PiLC is recording analog signals for the time the input GATE is in the high state. Depending on the requirements of the SAXS/WAXS experiments different trigger control modes can be realized at the beamline.

In the case of the very demanding SAXS/WAXS tensor tomography kind of experiment, an on-the-fly data trigger scheme has been implemented using special trigger pulses from the encoder position readout of the scanning linear stages from the company SmarAct®. These trigger pulses are fed into the master PiLC. The master PiLC puts the gate signal to the high state once the trigger pulse from the stage has a falling edge. Until the next position trigger pulse arrives the gate stays in the high state and the detectors and other devices are counting. Once the next trigger pulse arrives and has the rising edge the master PiLC switches the gate signal to a low state and the acquisition is stopped for all devices. Figure 6 (a) shows the trigger and produced gate signal for this measurement scheme. The user can adapt the exposure time for a virtual step of the continuous moving linear stage. The length of the trigger pulse from the encoder is fixed at 20 μ s. Typically, the exposure time of a virtual step is in the order of 20 ms. That means with a continuous motion mode operation data are collected more than 99.9% of the time. With this data acquisition mode, the fast shutter opens at the beginning of the continuous motion and closes after the whole motion is finished.

In the case of in-situ and anomalous SAXS/WAXS experiments, the triggering is time-based. In Figure 6 (b) an overview of the gate signals for this mode is shown. The user can define the length of the main exposure gate signal in the range of 4 ms – 600 s as well as the number of repetitions. This mode allows the definition of a delay time between two exposures. This delay time can be adjusted from 20 μ s – 600 s with a 1 μ s resolution. If the delay time is smaller than 5 ms the fast shutter will stay in the open position for all exposures and waiting times. In case the delay time is larger than 5

ms the fast shutter will be opened and closed for each exposure. To guarantee that the fast shutter is fully opened before the acquisition gate signal is set high, a second fast shutter control gate is produced by the master PiLC with some pre and post-offset times. This means the fast shutter starts opening roughly 2.5 ms before the main gate signal and starts closing roughly 1.5 ms after the main gate signal is finished. These two offset times can be adjusted as well.

3 Examples

3.1 ASAXS study of PVP-coated dried Au nanoparticles

To stabilize and prevent agglomeration of nanoparticles in solutions such as water special additives are added to the synthesis process (Stuart *et al.*, 2007; Liu *et al.*, 2022; Koczur *et al.*, 2015). These surfactants form a protecting layer around the primary nanoobject. Polyvinylpyrrolidone (PVP) is one often used additive that can act as a surface stabilizer, growth modifier, nanoparticle dispersant, and reducing agent (Koczur *et al.*, 2015). PVP prevents aggregation of nanoparticles via repulsive forces that arise from the hydrophobic carbon chains that extend into the solvents and interact with each other (steric hindrance effect (Quesada-Pérez *et al.*, 2021)). Due to the organic nature of those surfactant shells normally neutron scattering experiments are more suitable due to the higher scattering contrast for neutrons. In many cases, the scattering contrast of the organic shell is too weak to be detectable by X-ray scattering experiments. Recently a novel approach has been realized by combining small-angle neutron scattering (SANS) with small-angle X-ray scattering (SAXS) at one instrument (Metwalli *et al.*, 2020). However, the time resolution of SANS experiments is much lower compared to SAXS and the sample transmission has to be optimized for both X-rays and neutrons at the same time. Furthermore, other approaches could be used to vary the scattering contrast of the organic shell. This can be achieved by either using different solvents or by exploring the anomalous scattering effect in X-ray scattering experiments (Sakou *et al.*, 2013; Haas *et al.*, 2010; Vainio *et al.*, 2012; Hoell *et al.*, 2009).

The question is: Is it possible to detect an organic protecting shell around an inorganic metallic nanoparticle? To answer this question, we investigated a 5 nm diameter gold nanosphere covered by a PVP layer from the company NanoXact® using anomalous small angle X-ray scattering (ASAXS) at the Au-L3 X-ray absorption edge at the new beamline. The symbols in Figure 7 show the measured absolute differential scattering cross-section of the sample measured at six different X-ray energies below the Au-L3 X-ray absorption edge. A clear energy dependency of the intensity can be seen. The scattering curves have been normalized by the incoming photon flux and the sample transmission. The normalized intensity was subtracted by the normalized scattering intensity of an empty sample container as background. Finally, the intensity was normalized to absolute differential scattering units in cm^{-1} using the secondary standard sample glassy carbon (Zhang *et al.*, 2010; Dreiss *et al.*,

2006). Based on the TEM analysis of the NanoXact® company the particles can be assumed to be spheric with a certain size distribution. To check whether it is possible to detect the PVP shell, the scattering curves were modeled with two different models: (1) spherical particles with a log-normal size distribution and a structure factor to account for particle interaction and (2) spherical core-shell particles with a log-normal size distribution and a structure factor. Model 1 corresponds to the scenario that the PVP shell is not detectable by X-ray scattering and model 2 corresponds to the case that the PVP shell is detectable. The solid lines in Figure 7 show the modeled intensities. The quality of both non-linear regressions is very good. The quality is slightly better for the core-shell model (inset plot Figure 7 b) compared to that of the spherical particle model (inset plot Figure 7 a). A detailed description of the model equations and the fitting procedure is given in the supplementary information. The key advantage of the ASAXS modeling is that it is possible to perform a combined non-linear regression of all measured scattering curves at different energies. Because some model parameters such as radius, number density, etc. have to be energy independent the effective number of model parameters per scattering curve is reduced compared to a single curve fitting. In the case of the spherical model, the number of model parameters per curve is reduced from 10 parameters for the single fitting to effectively 4.2 parameters for the combined fit of 6 curves. In the case of the core-shell model, the number is reduced from 12 parameters to effectively 4.5.

Figure 8 shows the corresponding number density distribution as a function of particle radius. Both models give a very similar distribution with a mean value of the radius of 2.44 nm and a polydispersity of 9.8%. These values are in good agreement with the analysis from NanoXact® which reports a radius of 2.6 nm and a polydispersity of 12% based on the TEM analysis. To answer the question about the detectability of the PVP shell the energy-dependent scattering contrast of the core has to be analyzed in more detail. Figure 8 b shows the obtained scattering contrast as a function of X-ray energy for the pure spherical particle (black symbols) and the core of the core-shell particle (red symbols), respectively. The contrast values are higher for the spherical particle model compared to the core-shell model. In addition, the theoretical scattering contrast for gold against PVP as a function of X-ray energy was calculated and plotted in Figure 8 b as a reference (blue symbols). The agreement of the theoretical values is much better for the core-shell model compared to the pure spherical model. Therefore, the core-shell model is the better model assumption for modeling the measured SAXS curves. In conclusion, the ASAXS technique allows the detection of organic surfactant layers around metallic nanoparticles. This approach enables further X-ray studies on the effect of the protection layers on the performance of functionalized nanoparticles using in-situ and operando X-ray experiments such as in-situ ASAXS with a time resolution of a few seconds.

3.2 SAXS-CT of a phantom sample

To commission and optimize the measurement scheme and processing pipeline of the SAXS/WAXS tensor tomography experiments a phantom sample has been prepared and a full SAXS/WAXS computed tomography dataset has been collected at the SAXSMAT beamline. A detailed description and full data analysis will be published elsewhere. Here, only a few reconstructions will be discussed shortly. In Figure 9(a) a sketch of the phantom sample is shown. The different samples are placed in a solid water cube ($2.1 \times 2.1 \times 3.0 \text{ mm}^3$) with 0.3 mm diameter holes. Hereby, each sample has been placed in a 0.2 mm diameter Kapton tube with 0.025mm wall thickness. Solid water is a solid polymer that has the same electron density as liquid water. Different samples have been placed inside the phantom: amorphous Silica nanospheres with 120 nm diameter (Sigma Aldrich), crystalline ZnO nanoparticles with $\sim 20\text{nm}$ radius, collagen fibers, and carbon fibers. The collection was chosen such that each of them scatters at different q -values and has different scattering power or even orientations.

The SAXS/WAXS computed tomography dataset has been collected with the following experimental settings: X-ray energy = 11keV, beam size = $25 \times 10 \text{ }\mu\text{m}^2$, virtual step size of the vertical and horizontal directions = $30 \text{ }\mu\text{m}$, number of virtual translation steps in horizontal direction = 110 (continuous scan direction), number of translation steps in vertical direction = 115, number of rotation steps around the vertical axis = 61 (3.0° step size), and exposure time per virtual point = 50 ms. In total 771650 SAXS and 771650 WAXS patterns have been collected in $\sim 13\text{h}$. The dataset has been processed with an in-house developed processing pipeline, which will be described in a separate publication. In Figure 9(b) the reconstructed 3D tomogram of the SAXS intensity at $q=0.3\text{nm}^{-1}$ is shown in a 3D sliced view model. In the upper part of the volume, two crossing horizontal channels can be seen with higher intensity. These are carbon fibers. In the horizontal cutting plane at $z=1.2 \text{ mm}$ two round spots with higher intensities are visible. The spot at location (1.0,1.0,1.2) belongs to channel B which was filled with Silica nanoparticles. The second spot at (2.0, 2.0,1.2) mm belongs to channel D which was filled with ZnO nanoparticles.

A kind of reverse analysis can be done at any voxel of interest to retrieve the SAXS or/and WAXS scattering curve as a function of the scattering vector for that voxel. This scattering curve represents the scattering curve of only that particular voxel in the X-ray beam. Figure 9(c-e) are shown the obtained scattering curves for selected voxels. In Figures 9(c) and 9 (d) the curves for the two different fiber locations are shown as a function of the view angle ψ . The view angle is important for carbon fibers because they are highly oriented. For the fiber located in channel E (figure 9 (c) the SAXS and WAXS intensity is highest for the view angle $\psi = 0^\circ$ and lowest for $\psi = 90^\circ$. The broad peak around 18 nm^{-1} corresponds to carbon fiber. For the carbon fiber located in channel F, it is the opposite behavior because the channel is rotated by 90 degrees. In Figure 9 (e) the retrieved scattering curves for the location of the Silica NPs, ZnO NPs, and solid water matrix are shown. The

SAXS curves of the Silica NPs shows mainly the spherical form factor with a very narrow size distribution while the scattering curve of the ZnO particles represents particles with a much larger polydispersity as expected. The corresponding WAXS curves are also shown in Figure 9 (e). At $q = 22.5$ and 24.0 nm^{-1} two weak peaks are present in the ZnO location, indicating the presence of crystalline ZnO nanoparticles. On the other hand, no diffraction peaks were observed in the accessible region for the Silica NPs, indicating that the Si NPs are amorphous rather than crystalline. This example shows nicely the quality of the implemented SAXS/WAXS imaging setup at the new SAXSMAT beamline. A detailed description of the performance and data processing pipeline for the SAXS/WAXS tomography experiments at the SAXSMAT beamline will be published in a separate paper including a full analysis of the phantom sample concerning particle distribution, fiber orientation, and degree of alignment.

4 Summary

The new SAXSMAT beamline P62 at PETRA III is a versatile SAXS/WAXS instrument for applications of both hard and soft condensed matter research in the fields of chemistry, materials and life sciences, physics, and related disciplines. This manuscript describes the beamline's layout in terms of optics configuration and performance as well as the SAXS/WAXS instrumentation. The design parameters of the beamline were successfully achieved. In addition, two selected examples were shown to highlight the capability using the advanced techniques of anomalous scattering and computed tensor tomography that was realized at the beamline.

Acknowledgments

DESY is supported by the German Ministry for Research and Education (BMBF) within the Helmholtz Association. We would like to thank our colleagues from the DESY beamline technology, experimental computing, and undulator technology groups for their excellent support. Other beamlines at PETRA III are greatly acknowledged for discussions and collaborations.

Funding information

Funding for this project was provided by Ministry for Research and Education (BMBF), Helmholtz Association, and DESY.

References

- Baxter, R. J. (1970). *The Journal of Chemical Physics* **52**, 4559–4562.
- Blanchet, C. E., Spilotros, A., Schwemmer, F., Graewert, M. A., Kikhney, A., Jeffries, C. M., Franke, D., Mark, D., Zengerle, R., Cipriani, F., Fiedler, S., Roessle, M. & Svergun, D. I. (2015). *J Appl Crystallogr* **48**, 431–443.

- 1 Buffet, A., Rothkirch, A., Döhrmann, R., Körstgens, V., Abul Kashem, M. M., Perlich, J., Herzog, G.,
2 Schwartzkopf, M., Gehrke, R., Müller-Buschbaum, P. & Roth, S. V. (2012). *J Synchrotron Rad*
3 **19**, 647–653.
- 4 Conceição, A. L. C., Perlich, J., Haas, S. & Funari, S. S. (2020). *Biomedical Physics & Engineering*
5 *Express* **6**, 035012.
- 6 Dreiss, C. A., Jack, K. S. & Parker, A. P. (2006). *Journal of Applied Crystallography* **39**, 32–38.
- 7 Drube, W., Bieler, M., Caliebe, W. A., Schulte-Schrepping, H., Spengler, J., Tischler, M. & Wanzenberg,
8 R. (2016). Vol. p. 020035. New York, NY USA.
- 9 Franz, H., Leupold, O., Röhlberger, R., Roth, S. V., Seeck, O. H., Spengler, J., Strempler, J., Tischler, M.,
10 Viefhaus, J., Weckert, E. & Wroblewski, T. (2006). *Synchrotron Radiation News* **19**, 25–29.
- 11 Glatter, O. & Kratky, O. (1982). *Small Angle X-ray Scattering* Academic Press.
- 12 Guizar-Sicairos, M., Georgiadis, M. & Liebi, M. (2020). *J Synchrotron Rad* **27**, 779–787.
- 13 Haas, S., Fenger, R., Fertitta, E. & Rademann, K. (2013). *Journal of Applied Crystallography* **46**,
14 <https://doi.org/10.1107/S0021889813018190>.
- 15 Haas, S., Hoell, A., Wurth, R., Rüssel, C., Boesecke, P. & Vainio, U. (2010). *Physical Review B -*
16 *Condensed Matter and Materials Physics* **81**, <https://doi.org/10.1103/PhysRevB.81.184207>.
- 17 Hoell, A., Tatchev, D., Haas, S., Haug, J. & Boesecke, P. (2009). *Journal of Applied Crystallography* **42**,
18 323–325.
- 19 Jensen, T. H., Bech, M., Bunk, O., Menzel, A., Bouchet, A., Le Duc, G., Feidenhans'l, R. & Pfeiffer, F.
20 (2011). *NeuroImage* **57**, 124–129.
- 21 Koczkur, K. M., Mourdikoudis, S., Polavarapu, L. & Skrabalak, S. E. (2015). *Dalton Trans.* **44**, 17883–
22 17905.
- 23 Kristiansen, P., Horbach, J., Döhrmann, R. & Heuer, J. (2015). *J Synchrotron Rad* **22**, 879–885.
- 24 Krywka, C., Neubauer, H., Priebe, M., Salditt, T., Keckes, J., Buffet, A., Roth, S. V., Doebrmann, R. &
25 Mueller, M. (2012). *J Appl Crystallogr* **45**, 85–92.
- 26 Liebi, M., Georgiadis, M., Kohlbrecher, J., Holler, M., Raabe, J., Usov, I., Menzel, A., Schneider, P.,
27 Bunk, O. & Guizar-Sicairos, M. (2018). *Acta Crystallographica Section A Foundations and*
28 *Advances* **74**, 12–24.
- 29 Liebi, M., Georgiadis, M., Menzel, A., Schneider, P., Kohlbrecher, J., Bunk, O. & Guizar-Sicairos, M.
30 (2015). *Nature* **527**, 349–352.
- 31 Liu, D., Song, K., Chen, W., Chen, J., Sun, G. & Li, L. (2022). *Nuclear Analysis* **1**, 100011.
- 32 Metwalli, E., Götz, K., Lages, S., Bär, C., Zech, T., Noll, D. M., Schuldes, I., Schindler, T., Prihoda, A.,
33 Lang, H., Grassler, J., Jacques, M., Didier, L., Cyril, A., Martel, A., Porcar, L. & Unruh, T. (2020).
34 *J Appl Cryst* **53**, 722–733.
- 35 Pedersen, J. S. (1994). *Journal of Applied Crystallography* **27**, 595–608.
- 36 PyTango (2023). <https://pytango.readthedocs.io/en/stable/contents.html>.

- 1 Quesada-Pérez, M., Alberto Maroto-Centeno, J., Mar Ramos-Tejada, M. del & Martín-Molina, A.
2 (2021). *Physical Chemistry Chemical Physics* **23**, 14997–15002.
- 3 Sakou, M., Takechi, A., Murakami, S., Sakurai, K. & Akiba, I. (2013). *Journal of Applied Crystallography*
4 **46**, 1407–1413.
- 5 Sardana (2023). <https://www.sardana-controls.org/>.
- 6 Schaff, F., Bech, M., Zaslansky, P., Jud, C., Liebi, M., Guizar-Sicairos, M. & Pfeiffer, F. (2015). *Nature*
7 **527**, 353–356.
- 8 Schöps, A., Vagin, P. & Tischer, M. (2016). Vol. p. 020019. New York, NY USA.
- 9 Schulte-Schrepping, H., Degenhardt, M., Peters, H.-B., Hahn, U., Heuer, J. & Hesse, M. (2013). *J. Phys.: Conf. Ser.* **425**, 042005.
10
- 11 Schulte-Schrepping, H., Hesse, M., Degenhardt, M., Krüger, H., Peters, R., Peters, H. B. & Steffen, B.
12 (2016). Vol. p. 020041. New York, NY USA.
- 13 Sergueev, I., Döhrmann, R., Horbach, J. & Heuer, J. (2016). *J Synchrotron Rad* **23**, 1097–1103.
- 14 Studart, A. R., Amstad, E. & Gauckler, L. J. (2007). *Langmuir* **23**, 1081–1090.
- 15 Sztucki, M., Cola, E. D. & Narayanan, T. (2011). *Journal of Physics: Conference Series* **272**, 012004.
- 16 TANGO (2023). <https://www.tango-controls.org/>.
- 17 Tatchev, D. (2008). *Philosophical Magazine* **88**, 1751–1772.
- 18 Vainio, U., Lauten, R. A., Haas, S., Svedström, K., Veiga, L. S. I., Hoell, A. & Serimaa, R. (2012).
19 *Langmuir* **28**, 2465–2475.
- 20 Zhang, F., Ilavsky, J., Long, G. G., Quintana, J. P. G., Allen, A. J. & Jemian, P. R. (2010). *Metallurgical*
21 *and Materials Transactions A* **41**, 1151–1158.

22

23

24

25

1 Tables:

2 *Table 1: Specifications of beamline optics.*

Parameters	Specifications
Source	Undulator (U32)
Monochromator	Cryo-cooled DCM (Si(111) and Si(311))
Energy range (keV)	3.5 – 35.0
Mirror stripes	B ₄ C, Rh, Pt
Flux (photons s ⁻¹ @ 12 keV at 120 mA)	1.2 x 10 ¹³
Focus size at sample (H x V) (μm)	10 x 10 to 500 x 500

3

4 *Table 2: Specifications of the beamline photon source.*

Parameters	Specifications
Device length (m)	2.0
Period length (mm)	31.4
Peak field B ₀ (T)	0.91
Number of periods	61
Minimum magnetic gap (mm)	9.5
Deflection parameter K _{max}	2.7
Energy of 1 st harmonic (keV)	2.4

5

6 *Table 3: Summary of the DCM specifications.*

	travel range	repeatability	minimum step resolution
C1pitch (Bragg axis)	-3.0° - 40.0 °	< 0.20 μrad	< 0.10 μrad
C1roll	± 0.5 °	5.0 μrad	1.5 μrad
C2pitch	± 0.5 °	5.0 μrad	1.5 μrad
C2pitch-piezo	± 150 μrad	0.1 μrad	0.015 μrad
C2roll	± 0.5 °	5.0 μrad	1.5 μrad
C2x	10mm - 240 mm	2.5 μm	0.6 μm
C2z	10 mm – 30 mm	2.5 μm	0.6 μm

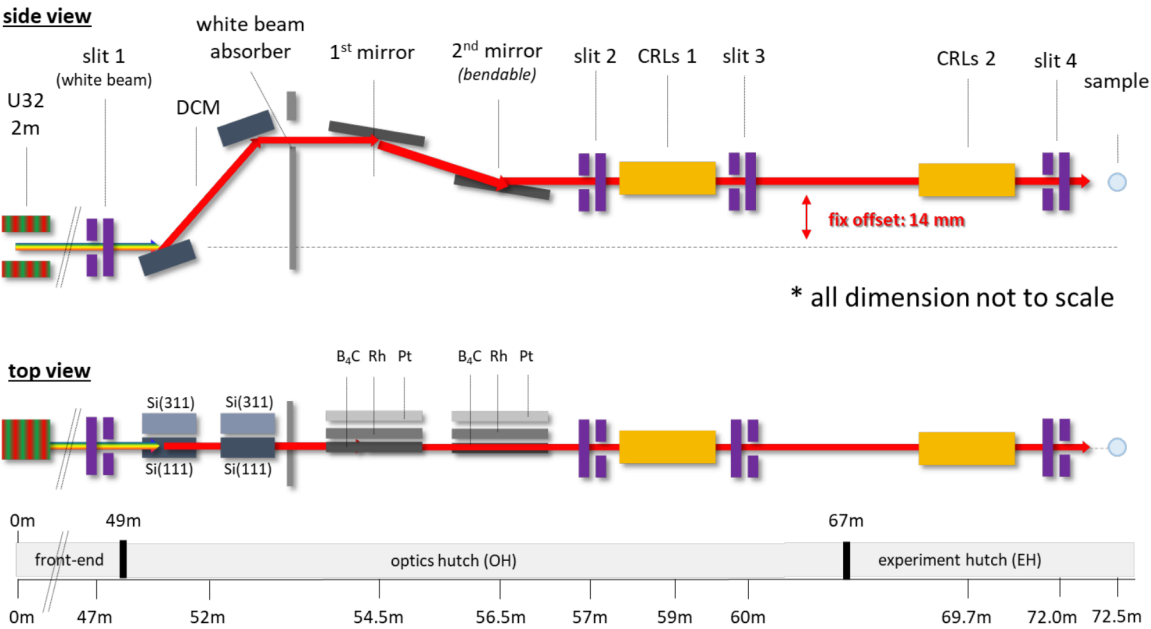
7

8

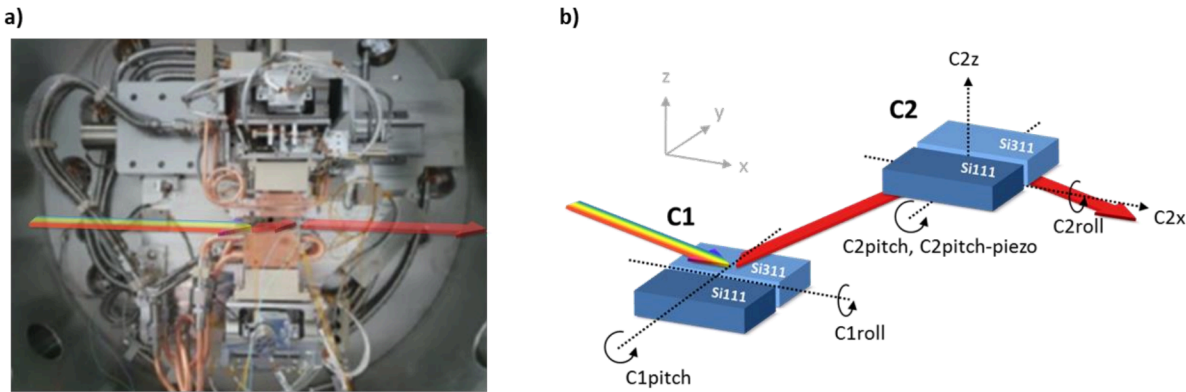
1 *Table 4: Specifications of the SAXS/WAXS instrument.*

Parameters	Specifications
X-ray energy range (keV)	3.5 – 35.0
Sample to SAXS detector distance (m)	1.9 – 13.0
Sample to WAXS detector distance (m)	0.2 – 0.5
Flux (photons s ⁻¹ @ 12 keV at 120 mA)	1.2 x 10 ¹³
Focus size at sample (H x V) (μm)	10 x 10 to 500 x 500
Beam stop diameter (mm)	4.5 and 6.0

3 *Figures:*



5 *Figure 1: Optics beamline layout with the main components. The intensity monitors, beam position screens, valves, pumps,*
6 *and diamond windows are not shown.*



9 *Figure 2: Photograph of the PETRA III high heat load monochromator. (b) Sketch of the translation and rotation degree of*
10 *freedom of the monochromator.*

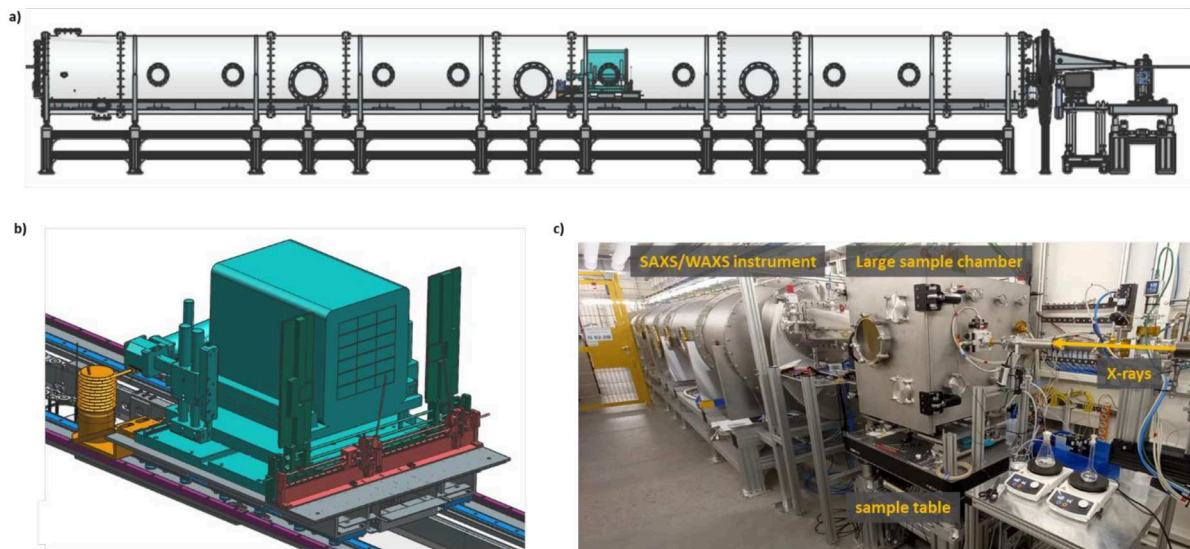


Figure 3: a) Side view of 3D CAD model of the SAXS/WAXS instrument. b) The SAXS detector mounting base with the additional beamstops and the protective cover. c) Photograph of the system in the experimental hutch.

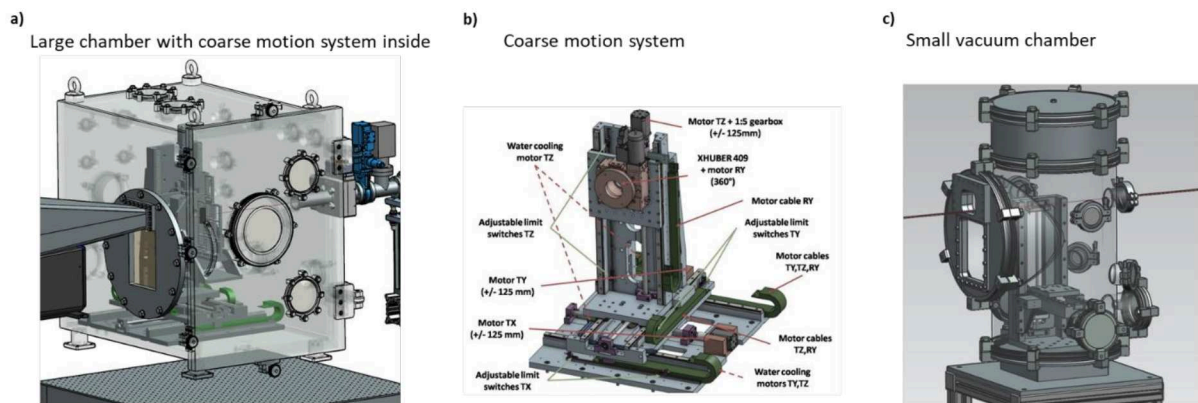


Figure 4: Sample environments. a) large chamber with a coarse motion system inside. b) Detailed view of the coarse motion system. c) Small vacuum chamber with limited motions inside.

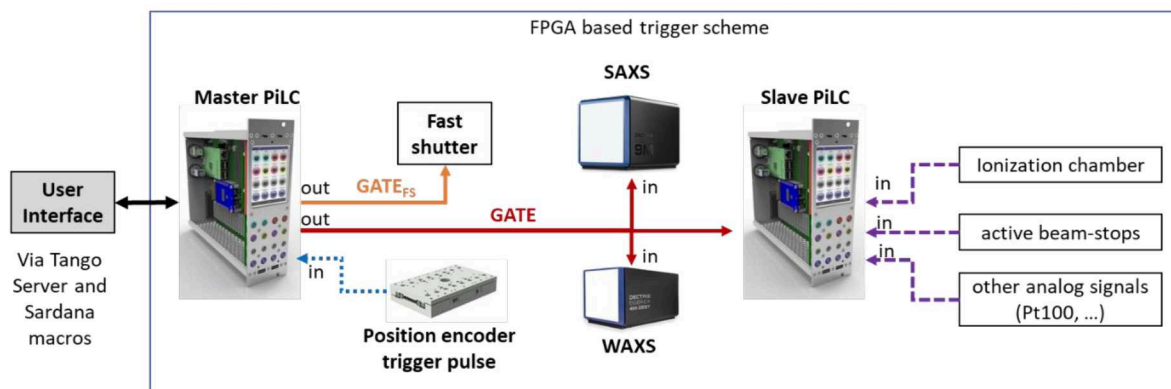
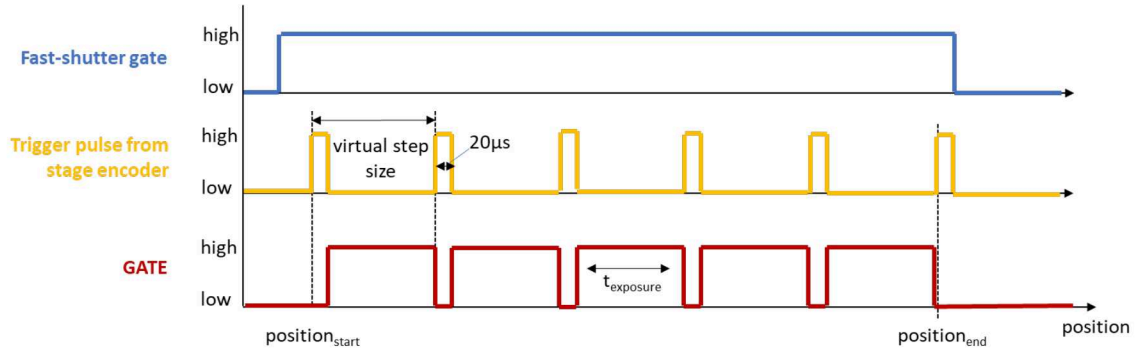


Figure 5: Simplified overview of the triggering scheme based on preprogrammed FPGAs.

1

a) Trigger scheme based on position encoder trigger pulses



b) Trigger scheme based on time

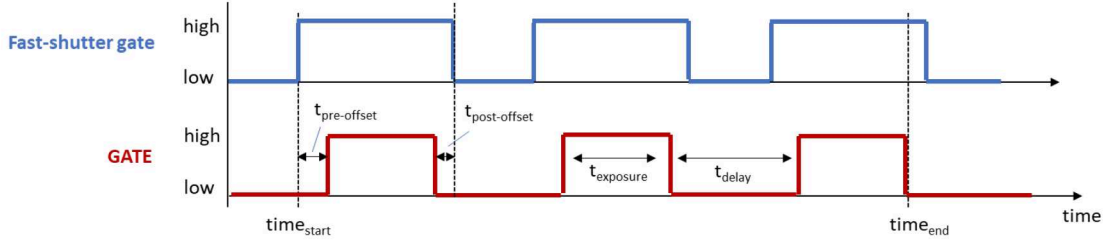
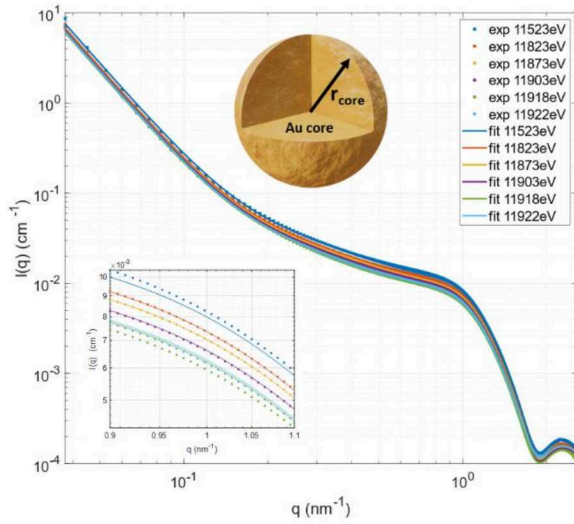


Figure 6: Trigger schemes implemented at the beamline. a) Trigger scheme based on trigger pulses from a position encoder electronic. b) Trigger scheme based on time.

a) Spherical shaped core particles



b) Spherical shaped core – shell particles

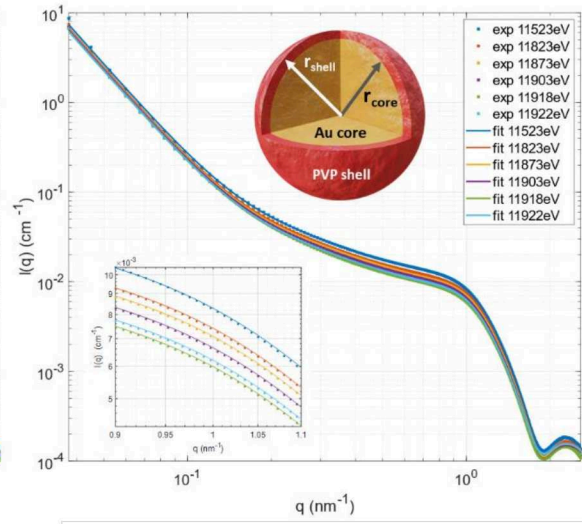


Figure 7: Experimental and modeled SAXS intensities using (a) polydisperse spherical-shaped particle, (b) polydisperse spherical-shaped core-shell particle model.

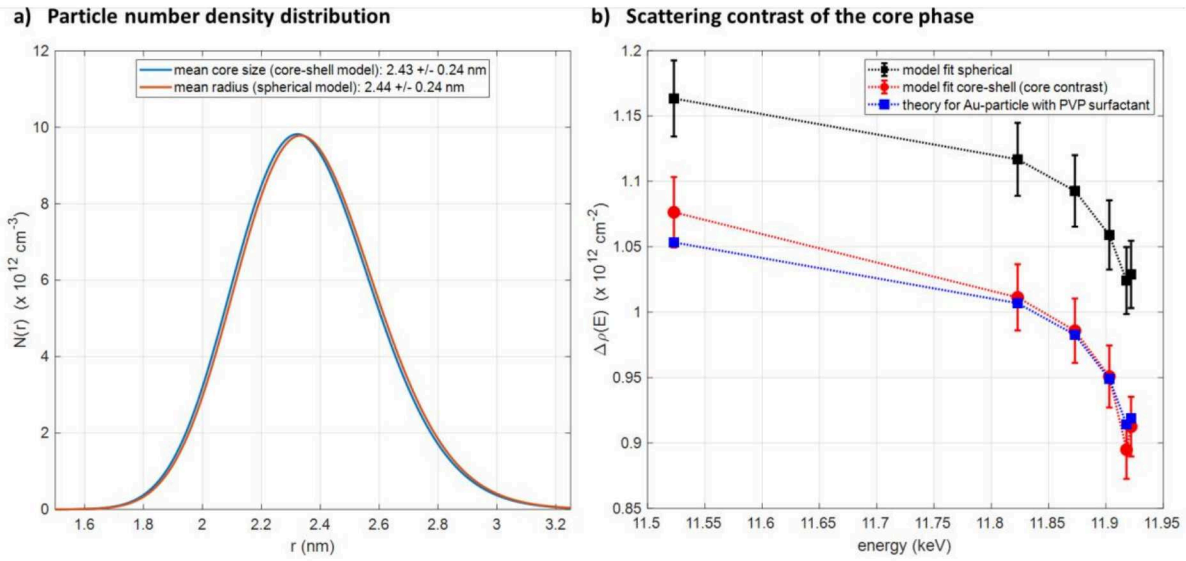


Figure 8: (a) Particle number density of both models. The mean radius is almost equal to 2.44 nm. (b) The energy-dependent scattering contrast of both models compared to the theoretical contrast for an Au core against a PVP shell. The symbols are the obtained values from the non-linear regression and the lines are linear interpolations of them for guidance only.

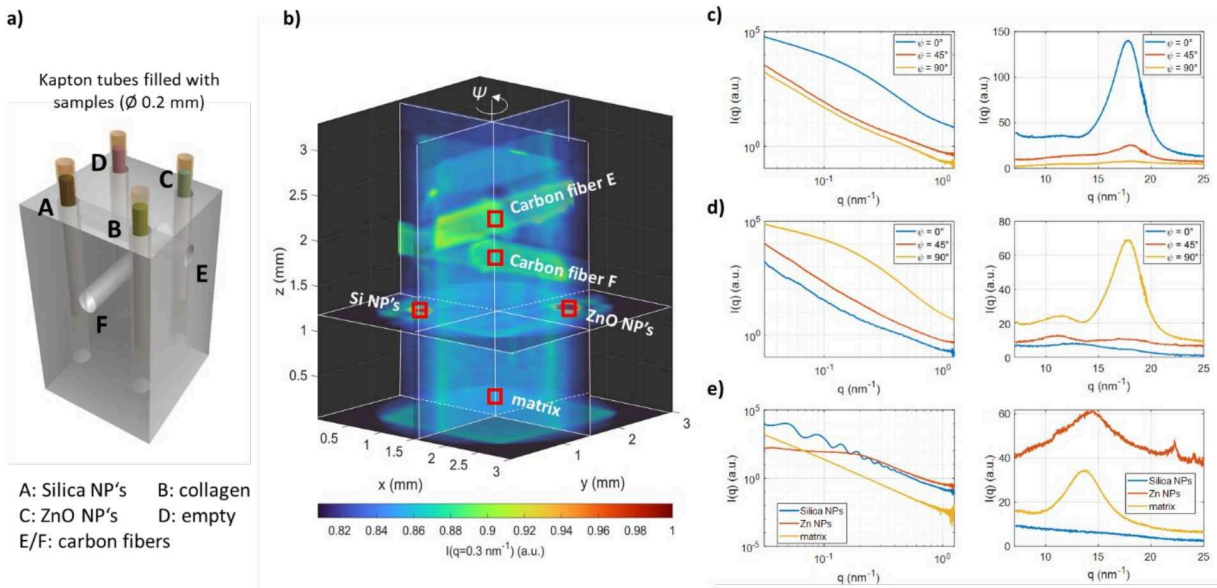


Figure 9: (a) Sketch of the phantom sample assembly. The Kapton tubes are filled with different samples (A = empty, B = Silica NPs, C = collagen lower part only, D = ZnO NPs, E & F = carbon fibers). (b) SAXS-CT reconstruction intensities at $q=0.3 \text{ nm}^{-1}$. Reconstructed SAXS & WAXS intensities of certain voxels: (c) carbon fiber location E as a function of view angle ψ , (d) carbon fiber location F as a function of view angle, (e) Si NPs, Zn NPs and solid water matrix locations.

Supplementary information

The new small angle X-ray scattering beamline for materials research at PETRA III: SAXSMAT beamline P62.

S. Haas^{a*}, X. Sun^a, A.L. Conceicao^a, J. Horbach^a, S. Pfeffer^a

^a Deutsches Elektronen-Synchrotron DESY, Notkestr. 85, 22607 Hamburg, Germany

*Correspondence e-mail: sylvio.haas@desy.de

1. Additional figures

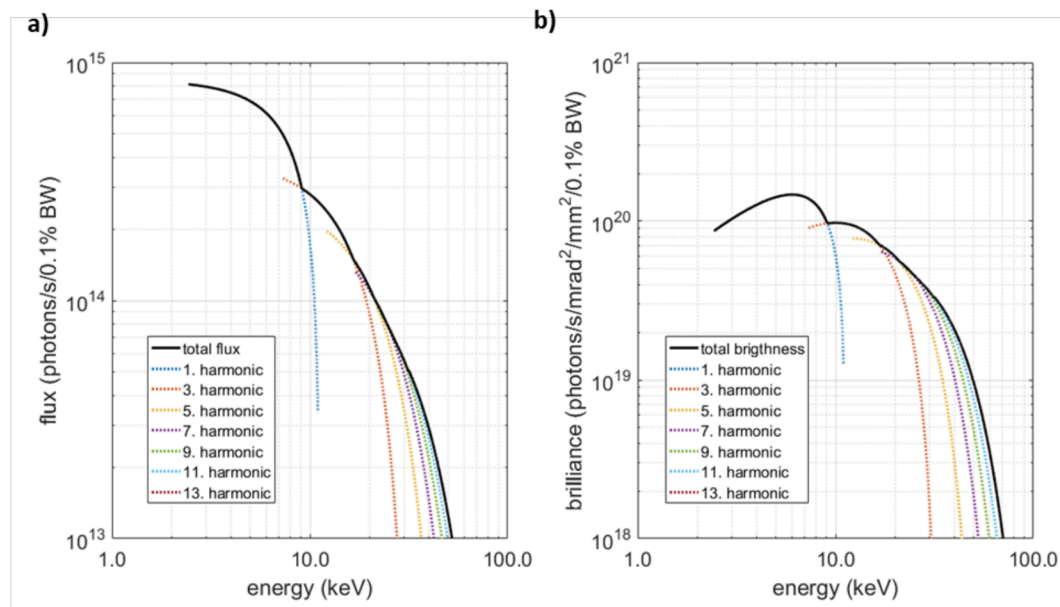


Figure S 1: Flux and brilliance of the U32 undulator of the SAXSMAT P62 beamline.

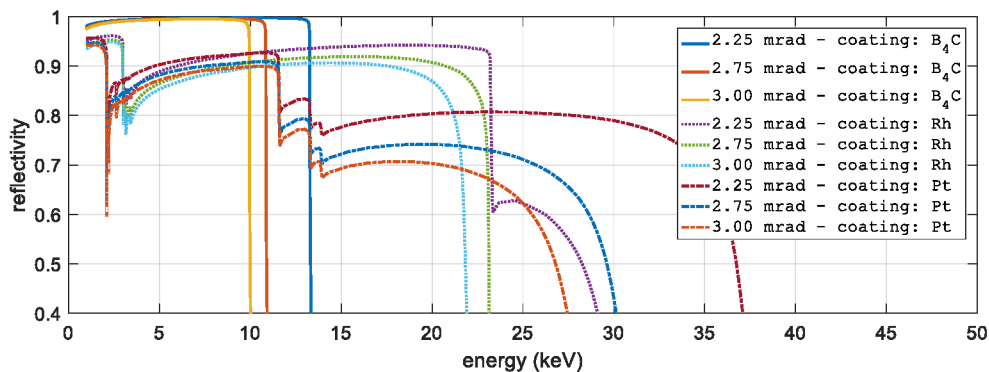


Figure S 2: Reflectivity curves of the double mirror system as a function of X-ray energy, pitch angle, and coating.

2. ASAXS study of PVP-coated dried Au nanoparticles

2.1. Spherical nanoparticle ASAXS model

The intensity of spherical nanoparticles with a lognormal size distribution and a structure factor in the local monodisperse approximation is given by (Glatter & Kratky, 1982; Pedersen, 1994):

$$I(q, E) = N \int_0^\infty P(r, \mu, \sigma) F_s(q, r, \rho(E))^2 S(q, r, rhs, \tau, \nu) dr + \beta_1(E) q^{-\alpha} + \beta_0(E).$$

N is the number density of particles in particles per cm^3 , μ and σ are the size distribution $P(r, \mu, \sigma)$ parameters (mean and polydispersity).

$F_s(q, r, \rho(E))$ is the form factor of spherical particles given by:

$$F_s(q, r, \rho(E)) = \frac{4}{3} \pi r^3 \rho(E) 3 \frac{\sin(qr) - qr \cos(qr)}{(qr)^3}.$$

$\rho(E)$ is the energy E dependent scattering contrast of the particle phase against the solvent.

As structure factor $S(q, r, rhs, \tau, \nu)$ the sticky hard sphere model has been used (Baxter, 1970). This model includes three additional model parameters: rhs is the repulsive radius, τ the stickiness parameter characterizing the adhesive strength, and ν is the local volume fraction of particles.

The scattering background is modeled by the last two terms including two energy-dependent parameters $\beta_0(E)$ and $\beta_1(E)$ and one energy-independent parameter α that should be between 3 and 4.

2.2. Spherical core-shell nanoparticle ASAXS model

The intensity of spherical core-shell nanoparticles with a lognormal size distribution and a structure factor in the local monodisperse approximation is given by (Glatter & Kratky, 1982; Pedersen, 1994):

$$I(q, E) = N \int_0^\infty P(r, \mu, \sigma) F_{cs}(q, r, d, \rho_{core}(E), \rho_{shell})^2 S(q, r, rhs, \tau, \nu) dr + \beta_1(E) q^{-\alpha} + \beta_0(E).$$

N is the number density of particles in particles per cm^3 , μ and σ are the size distribution $P(r, \mu, \sigma)$ parameters (mean and polydispersity).

$F_{cs}(q, r, d, \rho_{core}(E), \rho_{shell})$ is the form factor of spherical core-shell particles given by:

$$F_{cs}(q, r, d, \rho_{core}(E), \rho_{shell}) = F_s(q, r + d, \rho_{shell}) - F_s(q, r, \rho_{shell} - \rho_{core}(E)).$$

$\rho_{core}(E)$ is the energy E dependent scattering contrast of the particle core phase against the solvent and ρ_{shell} is the scattering contrast of the particle shell against the solvent phase, which can be assumed to be energy independent. In the present case water. d is the shell thickness.

As structure factor $S(q, r, rhs, \tau, \nu)$ the sticky hard sphere model has been used (Baxter, 1970). This model includes three additional model parameters: rhs is the repulsive radius, τ the stickiness parameter characterizing the adhesive strength, and ν is the local volume fraction of particles.

The scattering background is modeled by the last two terms including two energy-dependent parameters $\beta_0(E)$ and $\beta_1(E)$ and one energy-independent parameter α that should be between 3 and 4.

2.3. Summary of all fit parameters spherical model

parameter	E=11523eV	E=11823eV	E=11873eV	E=11903eV	E=11918eV	E=11922eV
α	3.52 ± 0.01					
β_0	0.0028 ± 0.0001	0.0022 ± 0.0001	0.0021 ± 0.0001	0.0021 ± 0.0001	0.0021 ± 0.0001	0.0036 ± 0.0001
β_1	0.0071 ± 0.0003	0.0064 ± 0.0002	0.0062 ± 0.0001	0.0061 ± 0.0001	0.0057 ± 0.0001	0.0058 ± 0.0001
N	5.734e-4 ± 5.97e-7					
μ	2.333 ± 0.001					
σ	0.0995 ± 0.0004					
ρ	1.163 ± 0.002	1.117 ± 0.003	1.093 ± 0.002	1.059 ± 0.001	1.024 ± 0.003	1.029 ± 0.002
rhs	3.628 ± 0.005					
τ	0.142 ± 0.002					
ν	0.069 ± 0.001					

The weighted R-value of the regression is: 0.0214425

2.4. Summary of all fit parameters spherical core-shell model

parameter	E=11523eV	E=11823eV	E=11873eV	E=11903eV	E=11918eV	E=11922eV
α	3.52 ± 0.01					
β_0	0.0021 ± 0.0002	0.0020 ± 0.0001	0.0020 ± 0.0001	0.0021 ± 0.0001	0.0028 ± 0.0001	0.0038 ± 0.0001
β_1	0.0070 ± 0.0002	0.0065 ± 0.0001	0.0063 ± 0.0001	0.0061 ± 0.0001	0.0058 ± 0.0001	0.0059 ± 0.0001
N	5.734e-4 ± 5.97e-7					
μ	2.323 ± 0.001					
σ	0.0998 ± 0.0004					
d	0.103 ± 0.012					
ρ_{core}	1.1864 ± 0.0002	1.1213 ± 0.0001	1.0958 ± 0.0001	1.0608 ± 0.0001	1.0049 ± 0.0001	1.0225 ± 0.0001
ρ_{shell}	0.11002 ± 0.00012					
rhs	3.626 ± 0.005					
τ	0.143 ± 0.002					
ν	0.070 ± 0.001					

The weighted R-value of the regression is: 0.0132957